

Power exhaust and core-divertor compatibility of the baffled snowflake divertor in TCV

S Gorno¹, C Colandrea¹, O Février¹, H Reimerdes¹, C Theiler¹, B P Duval¹, T Lunt², H Raj³, U A Sheikh¹, L Simons¹, A Thornton⁴, the TCV Team[‡] and the EUROfusion MST1 Team[§]

¹ Swiss Plasma Center (SPC), Ecole Polytechnique Fédérale de Lausanne (EPFL), Switzerland

² Max-Planck-Institut für Plasmaphysik, Garching bei München, Germany

³ Institute for Plasma Research, Gandhinagar, India

⁴ CCFE, Culham Science Centre, United Kingdom

E-mail: sophie.gorno@epfl.ch

November 2022

Abstract.

A baffled Snowflake Minus Low-Field Side (SF-LFS) is geometrically-optimised in TCV, increasing divertor neutral pressure, to evaluate the roles of divertor closure (comparing with an unbaffled SF-LFS) and magnetic geometry (comparing with a baffled Single Null, SN) in power exhaust and core-divertor compatibility. Ohmically-heated L-mode discharges in deuterium, with a line-averaged core density of approximately $4 \times 10^{19} \text{ m}^{-3}$, are seeded with nitrogen to approach detached conditions. Baffles in the SF-LFS configuration are found to reduce the peak outer target heat flux by up to 23%, without significantly affecting the location of the inter-null radiation region or the core-divertor compatibility. When compared to the baffled SN, the baffled SF-LFS exhibits a reduction in outer target heat flux by up to 66% and the ability to balance the strike-point distribution of heat flux. These benefits are less significant with N_2 seeding, with similar peak target quantities (such as heat flux, electron temperature and ion flux) and divertor radiated power. Despite a radiating region located farther from the confined plasma for the SF-LFS than the baffled SN, no change in core confinement is observed. Core effective charge even indicates an increase in core impurity penetration for the SF-LFS. These experiments constitute a good reference for detailed model validations and extrapolations, exploring important physics such as core impurity shielding and the dependence of divertor cross-field transport on magnetic geometry.

[‡] See author list of H. Reimerdes *et al.* 2022 *Nucl. Fusion* **62** 042018 (<https://doi.org/10.1088/1741-4326/ac369b>) for the TCV Team.

[§] See author list of B. Labit *et al.* 2019 *Nucl. Fusion* **59** 086020 (<https://doi.org/10.1088/1741-4326/ab2211>) for the EUROfusion MST1 Team.

1. Introduction

In future fusion devices, material limits will constrain reactor operation, highlighting divertor detachment as an essential operational regime [1, 2]. Divertor vs main chamber neutral compression has been identified as a key parameter in accessing divertor detachment [2]: future reactors will likely require operation at high divertor neutral pressures [1]. In TCV, regimes with enhanced divertor neutral pressure are achieved by increasing divertor closure with the installation of baffles [3, 4]. Alternative Divertor Configurations (ADCs) are being considered for future reactors to help mitigate heat fluxes arriving at the wall [5, 6, 7]. To this end, TCV's capacity to operate a wide range of ADCs has been enhanced by modifiable gas baffles [8].

One such ADC is the Snowflake Minus Low-Field Side (SF-LFS) configuration [9, 10], that features a secondary X-point in the LFS common flux region. The additional strike-points and extended region of low poloidal field in this geometry are modelled to increase divertor radiative losses and to lower target temperatures [11, 12, 13, 14]. A reduced peak outer target heat flux with respect to the standard Single Null (SN) configuration was already observed on TCV in the unbaffled SF-LFS, together with the ability to balance the ratio of power reaching each of the two active outer strike-points [15, 16].

Highly-radiative scenarios, achieved with impurity seeding, can greatly enhance divertor power dissipation. In the SN configuration, under detached conditions, an X-point radiator was observed with impurity seeding, where the dominant radiation is located in the vicinity of the X-point, reaching inside the confined region [17, 18, 19]. Conversely, nitrogen seeded experiments in the unbaffled SF-LFS featured a strongly radiating region between the two X-points [20], that was further from the core plasma than for the SN. Reactor relevance will require the core impurities to remain below some critical concentration in order to maintain fusion performance and plasma stability [21]. Therefore, assessing the impact of the radiation region displacement in the SF on core performance and core impurity levels is of high importance.

This study explores the performance of the baffled SF-LFS geometry, in terms of power exhaust and divertor-core compatibility, to appraise the combined effect of increased divertor closure and the complex magnetic geometry. In section 2, the development of the baffled SF-LFS configuration is described. The divertor conditions of this geometry are then determined, beginning in section 3 with a comparison of the target heat fluxes with baffled SN and unbaffled SF-LFS geometries. Section 4 explores the effect of

N₂ seeding on these divertor conditions, assessing both the effect on divertor radiated power and mitigation of target heat fluxes. Section 5 investigates the core-divertor compatibility of all configurations presented in this study, to compare the impact of magnetic geometries and divertor closures upon core impurity penetration and confinement. Finally, section 6 presents the key conclusions and outlook of this study.

2. Development of baffled SF-LFS configuration

The first generation of TCV baffles were designed to maximise the core-to-divertor neutral compression in the standard SN geometry whilst remaining compatible with a variety of other divertor geometries [8] (see for example the study of long-legged ADCs with baffles [22]). The SF-LFS features an even higher flux expansion in the null-point region than the SN, and so requires the development of a baffle-optimised geometry to maximise neutral compression whilst minimising plasma-baffle interaction. Two baffled SF-LFS geometries were developed with different X-point separations, together with a reference SN configuration, see figure 1 (a)-(c). The SF-LFS configuration increases the LFS connection length with respect to the SN, with no compromise on the HFS connection length, figure 1 (d)-(e). Note that the plasma volume is up to 5% lower in the SF-LFS compared to the SN.

An experimental database of discharges was constructed for each of these three geometries, with and without baffles, to explore the effect of increased divertor closure. In this section, the experimental set-up of these discharges is first outlined, followed by a description of the divertor diagnostics used within the study. We then assess the effectiveness of this geometric baffle-optimisation, by comparing the baffled geometries with their unbaffled counterparts and initial, non-optimised baffled SF-LFS discharges, in terms of divertor neutral pressure and plasma-baffle interaction.

2.1. Experimental set-up

The SF-LFS and SN configurations are ohmically-heated L-mode discharges in deuterium, with a plasma current $I_p = 245$ kA, operated in 'reversed' toroidal magnetic field (∇B ion drift directed upwards, away from the X-point) of $B_t = 1.44$ T, figure 2. This particular B_t direction was chosen to avoid the H-mode transition and to facilitate detachment at the outer divertor. The line-averaged core density is maintained at approximately $\langle n_e \rangle_l = 4.7 \times 10^{19} \text{ m}^{-3}$, corresponding to a Greenwald fraction of ~ 0.25 , figure

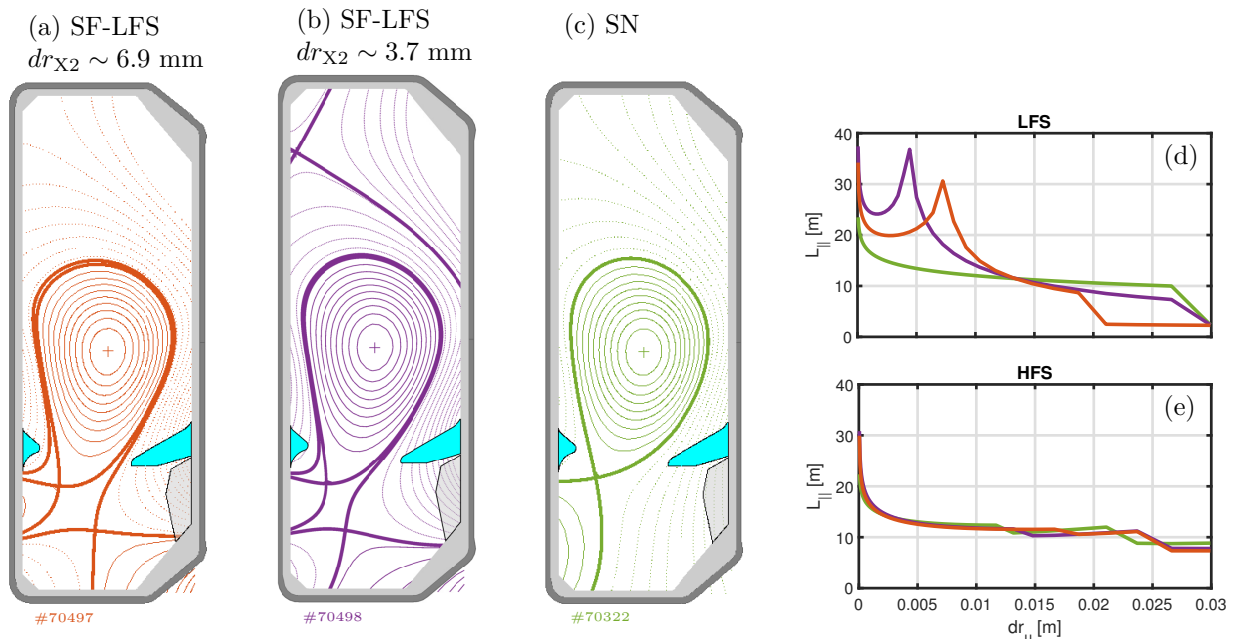


Figure 1: (a)-(c) Poloidal view of the magnetic equilibrium reconstructions of baffle-optimised geometries. For each geometry, the parallel connection length $L_{||}$ is given from the outboard midplane to the (d) LFS and (e) HFS targets, as a function of the upstream distance from the primary separatrix, dr_u , with colours corresponding to the magnetic equilibria in (a)-(c).

2 (d). N_2 is injected during the stationary phase of these discharges, to increase radiative cooling and approach detached conditions, figure 2 (f). Several discharges were performed in each configuration, baffled and unbaffled, to increase diagnostic coverage. With comparable core density and ohmic power traces in repeated discharges, we can compare these repeats for an indication of experimental reproducibility.

In the SF-LFS geometry, the secondary X-point causes the outer scrape-off layer (SOL) to split into two outer strike-points (OSPs) magnetically-connected to the SOL, referred to as SP2 and SP4 [11]. The X-point separation determines the power balance between SP2 and SP4 in attached conditions [15, 16], and is quantified by dr_{X2} , the distance between the two separatrices at the outboard midplane. Accordingly, two SF-LFS geometries with different dr_{X2} were developed to investigate the effect of divertor closure on the SF-LFS power sharing capability. The X-point separations in the baffled SF-LFS discharges are $dr_{X2} = 6.9 \pm 0.2$ mm and $dr_{X2} = 3.7 \pm 0.3$ mm (with errors corresponding to fluctuations within the discharge), figure 2 (c). The heat flux decay width, λ_q , of the reference SN geometry is ~ 3.9 mm [23]: comparatively, these SF-LFS geometries represent ‘large’ and ‘small’ X-point separations respectively. Unbaffled discharges were also performed for the same X-point separations, with $dr_{X2} = 6.6 \pm 0.7$ mm and $dr_{X2} = 3.0 \pm 0.5$ mm.

2.2. Divertor diagnostics

Figure 3 shows the poloidal position of the divertor diagnostics relevant to this study. The divertor neutral pressure is measured by a baratron pressure gauge at the divertor floor, shown in green in figure 3 (a). The D_2 and N_2 injection valves, that include flow measurements, are located either side of this pressure gauge.

Langmuir probes cover all strike-points and the plasma-facing sides of the baffles, and are operated in swept bias mode to measure ion saturation current density, j_{sat} , target electron temperature, T_e , floating potential, V_{fl} , and the electric current when grounded, j_0 , as detailed in [24, 25]. The target heat flux parallel to the magnetic field, $q_{||}$, can be calculated as the sum of contributions from electrons (e), ions (i) and the recombination process (rec), as performed in [26],

$$q_{||} = \underbrace{2T_e(j_{sat} - j_0)}_{q_{||,e}} + \underbrace{(2.5T_e + eV_{sh})j_{sat}}_{q_{||,i}} + \underbrace{E_{pot}j_{sat}}_{q_{||,rec}}, \quad (1)$$

where $E_{pot} = 15.8$ eV is the potential energy per incident ion, including the recombination energy and half the molecular bonding energy, and V_{sh} is the potential drop across the sheath,

$$V_{sh} = -\frac{1}{2} \ln \left(\frac{4\pi m_e}{m_i} \right) T_e + V_{fl}. \quad (2)$$

Here, we assume thermalisation between ions and electrons ($T_i = T_e$) and account for non-ambipolar

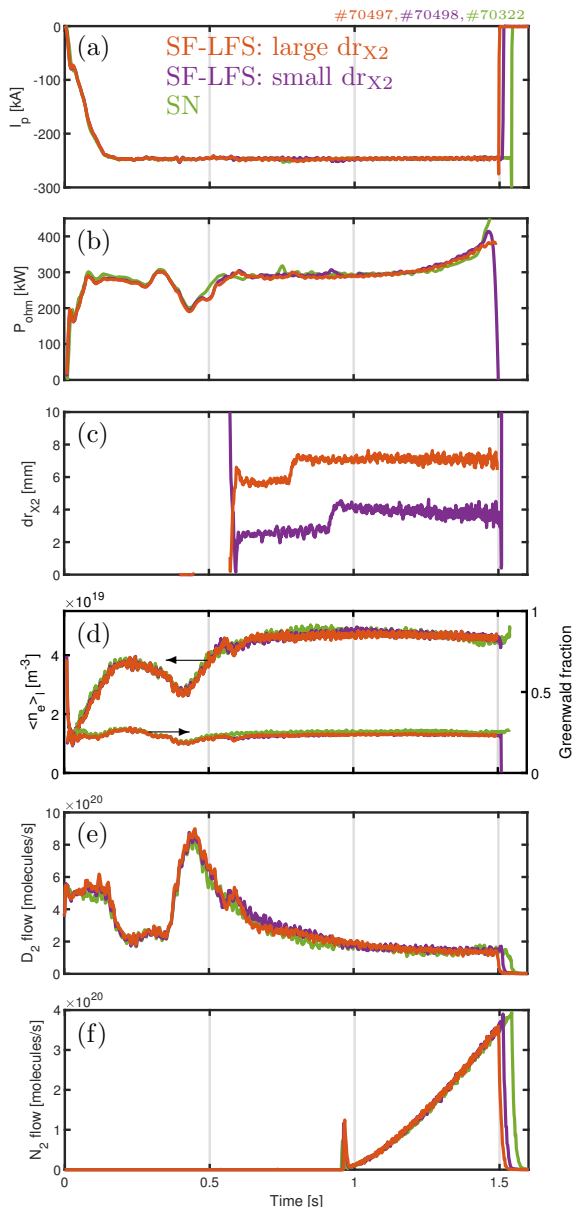


Figure 2: Typical time traces of (a) I_p , (b) P_{ohm} , (c) dr_{X2} , (d) $\langle n_e \rangle_1$ and the Greenwald fraction, and the injected gas flow of (e) D_2 and (f) N_2 for each of the three baffled magnetic geometries: large dr_{X2} SF-LFS (orange), small dr_{X2} SF-LFS (purple), SN (green). The SF shape is established at ~ 0.6 s, with the desired X-point separation obtained at ~ 0.80 s and ~ 0.96 s for the large and small dr_{X2} values, respectively.

conditions (non-zero SOL currents).

The target heat flux is also measured by the vertical (VIR) and horizontal (HIR) infrared systems, using the temperature variation of the machine wall tiles [23]. The fields of view of each system are portrayed in figure 3 (a). The HIR measures heat fluxes at SP1 and SP2 for the SF-LFS and the SN's

inner strike-point (ISP), whereas the VIR views the SN's OSP. Note that SP3 of the SF-LFS is inactive: it receives negligible heat and particle fluxes. IR measurements are used to complement the LP results, but remain incomplete as no IR data at SP4 is yet available.

In the following, we consider the target heat flux parallel to the magnetic field when comparing different divertor geometries, rather than that perpendicular to the target. The latter is strongly dependent on the incident magnetic field line angle, which is a function of both poloidal target flux expansion and wall tilt [7]. As the wall tilt is not optimised for the different configurations in this study, comparisons of the perpendicular heat flux could be misleading. The parallel heat flux profiles from both LPs and IR are plotted in this work as a function of the normalised poloidal magnetic flux, $\rho_\psi = \sqrt{(\psi - \psi_0)/(\psi_{LCFS} - \psi_0)}$, where ψ is the poloidal magnetic flux and ψ_0 and ψ_{LCFS} are inferred at the magnetic axis and at the last closed flux surface (primary separatrix) respectively.

The plasma radiated power is measured by a recently-upgraded bolometry system, RADCAM [27], with coverage of both the core and divertor regions of TCV (see figure 3 (b)). This system is used for the baffled discharges outlined above, but was not yet available for the older, unbaffled discharges.

2.3. Geometric baffle-optimisation

An optimal distance between the SOL and LFS baffle exists where the divertor neutral pressure is maximised, due to competition between divertor closure and plasma-baffle interaction. Increasing further the SOL proximity to the LFS baffle increases the plasma recycling flux on the baffle and reduces divertor neutral pressure, weakening the benefit of gas baffles [28]. The SOL-baffle proximity is strongly affected by the plasma vertical position within the vessel, core plasma shape and dr_{X2} . Thus, baffle-optimised SF-LFS geometries were designed to maximise the SOL-baffle distance, while maintaining a sufficiently large dr_{X2} to approach a balanced peak heat flux distribution at the OSPs. This involved reducing the lower core width, hence decreasing plasma volume and increasing elongation, while shifting the X-points towards the HFS.

For the baffle-optimised SF-LFS geometries, the divertor neutral pressure approximately doubles compared to the equivalent unbaffled geometry (shown in figure 4), similarly to the baffled standard SN configuration at these upstream conditions [3]. This difference is maintained throughout the discharges, even when seeding N_2 into the divertor. The first attempts of baffled SF-LFS discharges, that were not baffle-optimised, have comparable divertor neutral

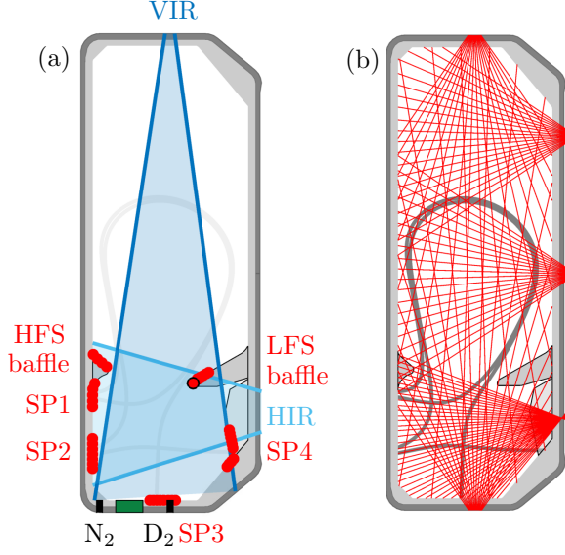


Figure 3: Poloidal cross-section of the TCV vessel with the divertor diagnostics relevant to this study overplotted, (a): Langmuir probes (red markers); vertical (VIR) and horizontal (HIR) infrared fields of view (blue areas); gas valves for D_2 and N_2 injection (black boxes); and pressure gauge (green box); (b): RADCAM bolometer lines of sight.

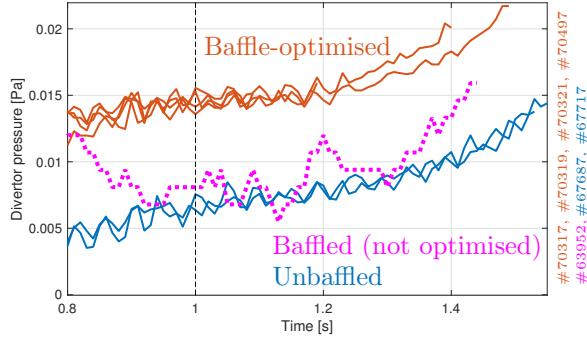


Figure 4: Divertor neutral pressure measurements from the divertor floor pressure gauge for the unbaffled (blue), baffled but not optimised (magenta) and baffle-optimised (orange) SF-LFS configurations. The vertical dashed line at 1s represents the beginning of a N_2 seeding ramp. Results are shown from repeat discharges in each geometry.

pressure to the unbaffled cases, demonstrating the need for attentive geometric optimisation.

As expected, the baffle-optimisation also strongly reduces the particle flux impinging the plasma-facing side of the LFS baffle. In the baffle-optimised SF-LFS geometry, the magnetic flux surface $\rho_\psi \sim 1.07$ (corresponding to an upstream distance from the separatrix of $dr_u \sim 22$ mm) is intercepted by the LFS

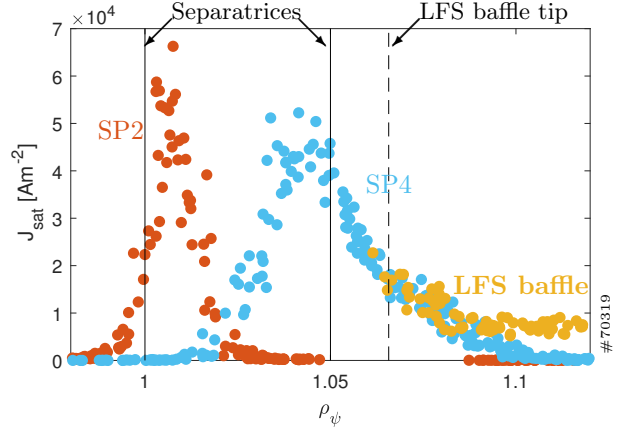


Figure 5: Profiles of the ion saturation current density parallel to the magnetic field (j_{sat}) measured by LPs at the LFS baffle and active outer strike-points (SP2, SP4) of the baffle-optimised SF-LFS configuration with $dr_{X2} \sim 6.9$ mm. The separatrixes are indicated by solid lines and the position of the LFS baffle tip is indicated by a dashed line, at $\rho_\psi = 1.069 \pm 0.005$.

baffle tip (see figure 5). By contrast, for the geometry which is not baffle-optimised, the baffle tip intercepts $\rho_\psi \sim 1.04$ (correspondingly $dr_u \sim 12$ mm), being much closer to the core plasma (not shown). The ion flux recycled at the plasma-facing LFS baffle surface is considerably reduced by the geometric optimisation, becoming comparable to that of the reference SN (in which the LFS baffle tip intercepts $\rho_\psi \sim 1.09$, $dr_u \sim 27$ mm).

Note that the HFS baffle interaction remains negligible for all baffle-optimised geometries. The baffle-optimised SF-LFS configuration thus allows for a fairer comparison of target behaviour between configurations.

3. Target conditions of the baffled SF-LFS

In the SF-LFS geometry, the power distribution between the active outer strike-points depends upon the X-point separation: the higher dr_{X2} , the higher the ratio of the heat fluxes reaching SP2 to SP4. Of the two SF-LFS geometries considered in this study (see figure 1), the case with $dr_{X2} \sim 3.7$ mm presents a more balanced peak heat flux ($q_{\parallel}^{\text{peak}}$) distribution between the outer targets, while the case with $dr_{X2} \sim 6.9$ mm presents a higher $q_{\parallel}^{\text{peak}}$ at SP2 than SP4.

Compared with the baffled SN, a reduction in $q_{\parallel}^{\text{peak}}$ is observed at the outer divertor in the baffle-optimised SF-LFS (see figure 6 (a)-(b)), as seen in previous studies without baffles in TCV [15] and in NSTX [29]. Note that while the LPs and IR show

fair agreement for measured q_{\parallel} profiles, discrepancies remain in the magnitude of $q_{\parallel}^{\text{peak}}$, with the VIR reporting generally higher and the HIR generally lower values than the LP-measured $q_{\parallel}^{\text{peak}}$. Despite the difference in magnitude, the LPs and IR show consistent trends in target heat flux with varying divertor geometry. The SF-LFS case with $dr_{X2} \sim 3.7$ mm presents a significant parallel heat flux reduction in the outer divertor with respect to the SN configuration, with IR measuring a reduction of 66% and LPs of 57%. For the SF-LFS case with larger X-point separation ($dr_{X2} \sim 6.9$ mm), IR sees a reduction of 59%, and LPs of 24%. This heat flux reduction coincides with a reduction in the $\Gamma_{\parallel}^{\text{peak}}$ and V_{sh} , rather than a strong reduction in T_e^{peak} . Furthermore, this reduction with respect to the SN is stronger for the SF-LFS with small dr_{X2} since the heat fluxes at SP2 and SP4 are more balanced. For the remainder of this paper, the focus will be placed upon the case with $dr_{X2} \sim 6.9$ mm, while the small dr_{X2} case will be used to investigate the generality of results to the SF-LFS.

When compared with the unbaffled configuration, the baffle-optimised SF-LFS presents a $q_{\parallel}^{\text{peak}}$ reduction of $\sim 18\%$ at SP2 and $\sim 23\%$ at SP4, as shown in figure 6(c). LP data suggest that this reduction coincides strongly with a reduction in T_e^{peak} , as seen for increasing divertor closure in JT60U and Alcator C-mod [30, 31], with no strong change in $\Gamma_{\parallel}^{\text{peak}}$. This is also seen for the SF-LFS case with small dr_{X2} (not shown here), and is therefore assumed to be a general feature of the SF-LFS configuration. Over the range $dr_{X2} = [2.0, 7.1]$ mm, the baffles reduce $q_{\parallel}^{\text{peak}}$ almost symmetrically at each active outer strike-point, so the dependence of outer target $q_{\parallel}^{\text{peak}}$ distribution on dr_{X2} is largely unaffected by baffles.

At the inner target, we note that all configurations exhibit comparable q_{\parallel} profiles, demonstrating that the outer target q_{\parallel} is not simply reduced from the change in in-out power sharing with changing geometry. We conclude that the baffled SF-LFS exhibits a clear peak outer target heat flux reduction, with respect to both the unbaffled SF-LFS and the baffled SN in the absence of N_2 injection.

4. Evolution of divertor conditions with N_2 seeding

The mitigation of target heat flux requires significant radiative losses in the divertor, which can be increased by impurity seeding. In this section, the effect of N_2 injection on the target heat fluxes and divertor radiated power is reported. The time-integrated N_2 flux is used as a proxy for divertor N_2

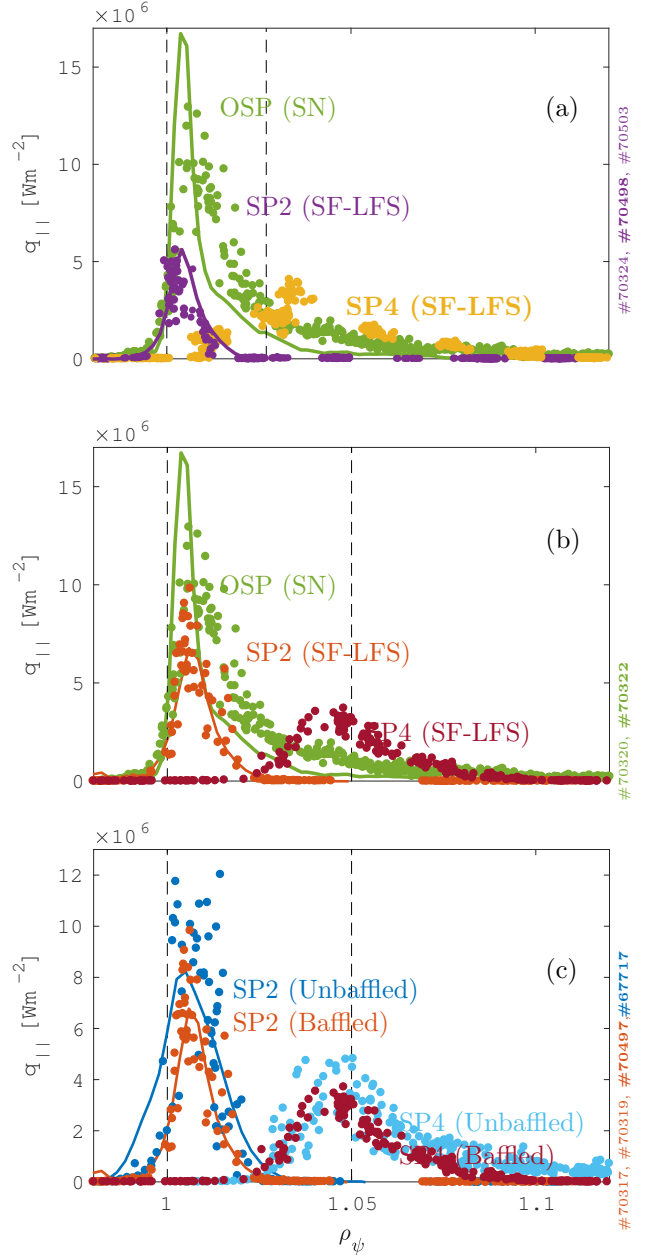


Figure 6: Outer target heat flux profiles of the active outer strikepoints of the following geometries prior to any N_2 injection, measured by the LPs (markers) and the IR (solid lines): (a) the baffle-optimised SF-LFS ($dr_{X2} \sim 3.7$ mm) compared with the baffled SN; (b) the baffle-optimised SF-LFS ($dr_{X2} \sim 6.9$ mm) compared with the baffled SN; (c) the baffle-optimised SF-LFS ($dr_{X2} \sim 6.9$ mm) compared with the unbaffled counterpart. The dashed lines represent the positions of the primary and secondary separatrixes of the SF-LFS.

content, since the absolute divertor N_2 concentration cannot yet be measured on TCV. This quantity represents an upper limit for the divertor N_2 content, as it accounts for neither wall-retention, exhaust to the TCV pumps nor core penetration of the impurity, which cause the actual divertor N_2 content to be lower. Nevertheless, it is considered a useful parameter in comparing the detachment properties of the different configurations. In these scenarios, only partial detachment [32] can be achieved, as N_2 causes plasma disruption before pronounced detachment. The lowest T_e^{peak} measured is 6.2 eV, similar to the minimum target temperatures measured in other N_2 seeding experiments on TCV [19].

4.1. Target heat flux mitigation

In all configurations, a general decrease in peak target ion flux ($\Gamma_{\parallel}^{\text{peak}}$), electron temperature (T_e^{peak}) and heat flux ($q_{\parallel}^{\text{peak}}$) is observed in the outer divertor with N_2 injection as the outer divertors begin to detach (see figure 7). In the baffled SF-LFS, LP-measured $q_{\parallel}^{\text{peak}}$ decreases strongly with the start of N_2 seeding, but quickly plateaus to an approximately constant value of $2.3 \pm 0.3 \text{ MWm}^{-2}$. This represents the overall peak of the outer targets, which for the SF-LFS is the maximum of SP2 and SP4, and for the SN is simply the OSP peak. Peak target temperature and ion flux behave similarly, attaining approximately constant values of $8.2 \pm 1.0 \text{ eV}$ and $(2.1 \pm 0.2) \times 10^{23} \text{ m}^{-2}\text{s}^{-1}$ respectively. Impurity seeding strongly reduces $q_{\parallel}^{\text{peak}}$ at SP2, which is connected to the near SOL, but has a smaller effect at SP4, which is connected to the far SOL. For a time-integrated N_2 flow of approximately 3×10^{19} molecules, $q_{\parallel}^{\text{peak}}$ at SP2 becomes lower than at SP4, while at SP4 $q_{\parallel}^{\text{peak}}$ decreases very little with further N_2 injection. Divertor cooling with N_2 injection increases the neutral mean free path, potentially allowing neutrals to travel further into the confined plasma rather than remaining, and dissipating power, in the divertor. This may explain the observed $q_{\parallel}^{\text{peak}}$ stagnation. Figure 7 (a) also displays IR-measured $q_{\parallel}^{\text{peak}}$, but only for SP2 as data is not available for SP4. From a time-integrated N_2 flow of $\sim 3 \times 10^{19}$ molecules, the IR data is marked by a dashed line for the SF-LFS configurations, as the SP2 peak is no longer expected to represent the overall peak of the outer targets. The IR data before this line is in fair agreement with the LPs, within the experimental scatter.

When compared with the unbaffled SF-LFS, the baffled SF-LFS exhibits a clear decrease in $q_{\parallel}^{\text{peak}}$ from zero to moderate levels of N_2 seeding, coincidentally with a reduction in T_e^{peak} . For high injection levels of N_2 , the difference in both $q_{\parallel}^{\text{peak}}$ and T_e^{peak} between

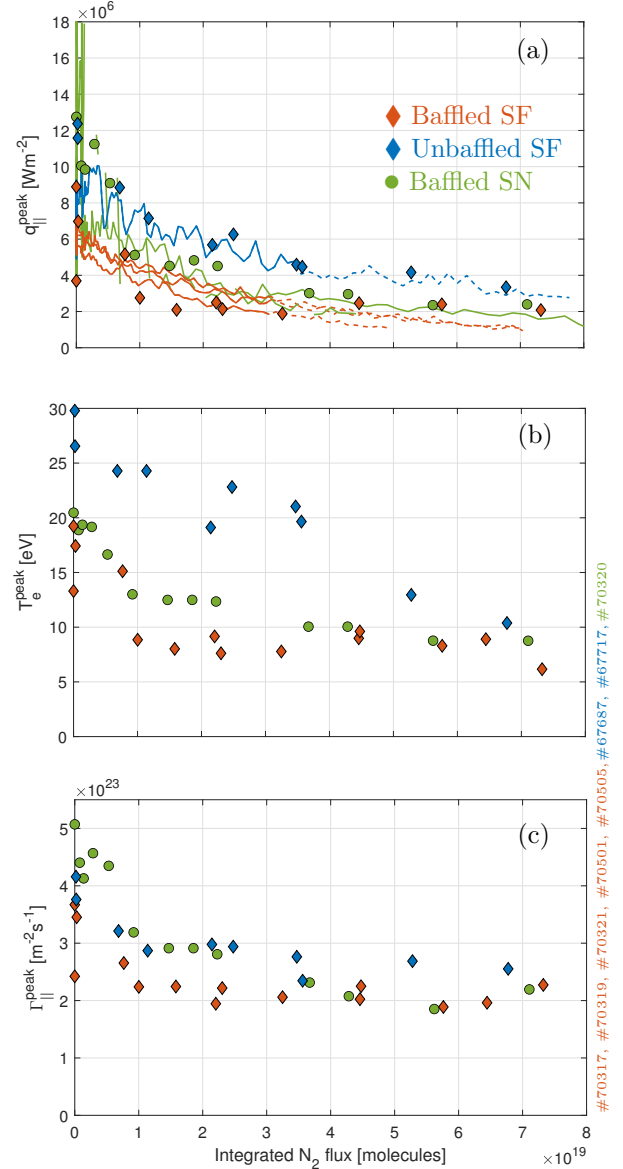


Figure 7: Peak outer target (a) parallel heat flux, (b) electron temperature, (c) parallel ion flux, plotted as a function of the time-integrated N_2 flux. Data measured by LPs (markers) present the overall outer target peak value (considering both SP2 and SP4 for the SF-LFS), whereas heat flux data measured by IR (lines) consider only SP2, as SP4 data is not available. Dashed lines indicate where the outer target heat flux is expected to peak at SP4. Results are shown from repeat discharges in each geometry to give an indication of experimental reproducibility.

the configurations is reduced, where the unbaffled SF-LFS displays continuous reductions, but the values remain constant in the baffled SF-LFS. The colder baffled divertor may reduce the radiative efficiency of N_2 , hence stagnating the reduction of peak target heat

flux. This will be discussed further in the following sub-section. However, the stagnation of electron temperature may also be due to a limitation in the LP measurement, where a modification of the plasma resistance or fluctuations in the floating potential may lead to an over-estimation of the electron temperature in detached conditions [33].

Compared with the baffled SN, we see a clear reduction of $q_{\parallel}^{\text{peak}}$ in the baffled SF-LFS until a time-integrated N_2 flux of $\sim 4 \times 10^{19}$ molecules. This heat flux reduction comes with only a slight reduction in T_e^{peak} — the presence of baffles appears to have a stronger effect on T_e^{peak} than this change in magnetic geometry. Injecting additional N_2 tends to make $q_{\parallel}^{\text{peak}}$ equal for the two configurations, along with $\Gamma_{\parallel}^{\text{peak}}$. Note that the stagnation of $q_{\parallel}^{\text{peak}}$ with N_2 seeding in the baffled SN occurs at a higher quantity of injected N_2 than for the baffled SF-LFS. The reason for the equivalence of target heat flux between geometries with strong N_2 seeding is not currently understood. This could be an indication of lower divertor N_2 retention in the SF-LFS compared to the SN.

At the inner strike-point, the peak target heat flux is comparable across all geometries, including those with N_2 injection. We conclude that the heat flux reduction observed in the baffled SF-LFS with respect to all other cases is not simply due to a redirection of power to the inner target.

4.2. Divertor radiated power

The plasma emissivity calculated from tomographic inversions [34] of the bolometry data gives an indication of regions of strong radiated power, as shown in figure 8. The baffled SF-LFS exhibits a radiation region between the two X-points, whereas an X-point radiator is seen for the baffled SN configuration. The inter-null radiation region is observed in the SF-LFS for both X-point separations, with and without baffles, and before and during the N_2 -seeded phase of the discharge (the small $dr_{\text{X}2}$ and unbaffled cases are not shown here). This broadly distributed radiation region in the SF-LFS is also observed in previous TCV experiments [20], as well as in other SF configurations and in other tokamaks [29, 35, 36]. This is therefore a key feature of the SF geometry. These regions increase in size and intensity with N_2 seeding, moving closer to the confined plasma region, as apparent in figure 8.

The radiated exhaust power, P_{rad} , is calculated by integrating the plasma emissivity over the divertor volume and X-point region (see yellow region inset in figure 9). To account for small variations in the Ohmic heating power and core conditions in each configuration, we compare the radiated power fraction, by evaluating the ratio of P_{rad} to the power entering

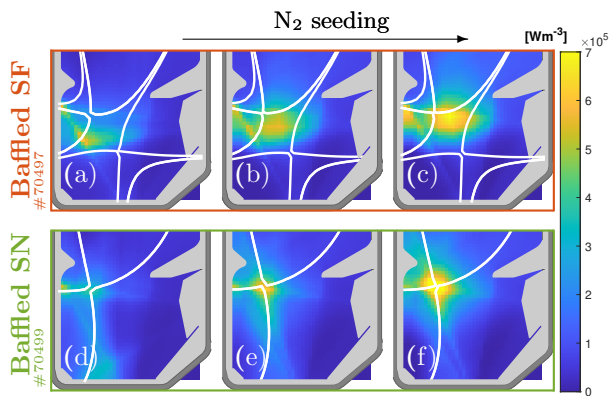


Figure 8: Poloidal plots of plasma emissivity from bolometry for (a)-(c): the baffled SF-LFS, and (d)-(f): the baffled SN configurations. From left to right, the quantity of time-integrated N_2 flux is increased: (a),(d): ~ 0 molecules; (b),(e): $\sim 3.0 \times 10^{19}$ molecules; (c), (f): $\sim 6.0 \times 10^{19}$ molecules.

the SOL, P_{SOL} . P_{SOL} is the input (Ohmic) heating power minus the core radiated power. For simplicity, the core is defined as the region above the HFS baffle tip, as shown by the purple region inset in figure 9, excluding the X-point region while fairly comparing two magnetic geometries with different core shapes. The divertor radiated power fraction thus obtained (figure 9) is at most 10% higher in the baffled SF-LFS than in the baffled SN configuration, up to a time-integrated N_2 flux of approximately 4×10^{19} molecules. This is consistent with the 10-15% difference in divertor radiated power measured in DIII-D [37]. Similar values are obtained for the small $dr_{\text{X}2}$ case (not shown) within the experimental scatter. However, the uncertainty associated with the divertor bolometric inversions for these discharges is around 10%, and so no strong difference in P_{rad} can be concluded between the two configurations.

5. Core-divertor compatibility

As part of the assessment of the SF-LFS configuration as a potential divertor solution for future reactors, we must consider divertor-core compatibility alongside power exhaust enhancements, to limit core impurity pollution and the degradation of energy confinement. Two complementary metrics will be used in this assessment: the core effective charge and the main plasma energy confinement time.

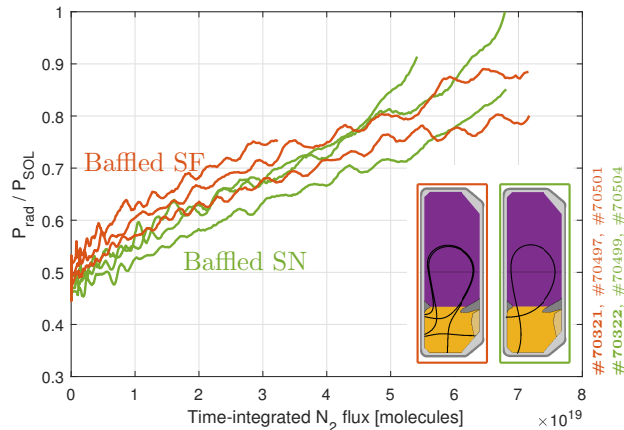


Figure 9: Bolometry data from the recently-installed RADCAM system showing the proportion of the power entering the SOL, P_{SOL} , that is radiated in the divertor and X-point region for the baffled SF-LFS and SN configurations. Results are shown from repeat discharges in each geometry. Inset, for each magnetic geometry, the regions corresponding to the core (purple) and divertor/X-point region (yellow) for the purpose of the radiated power fraction calculation are shown.

5.1. Core effective charge

The core effective charge is defined in the usual manner as,

$$Z_{\text{eff}} = \frac{\sum_i n_i Z_i^2}{n_e}, \quad (3)$$

where n_i is the density of each ion species i and Z_i is the charge number of that species. Z_{eff} is estimated from measurements of V_{loop} and the profile-averaged core temperature from Thomson scattering, assuming steady state conditions and neo-classical conductivity [38, 39].

The core effective charge is shown in figure 10 (a), as a function of the time-integrated N_2 flux. Initially, Z_{eff} is only slightly above 1, the value of an undiluted deuterium plasma, but then increases once N_2 seeding begins. Measurements of core carbon density suggest that this increase in Z_{eff} is in fact due to an increase in core nitrogen content, rather than a variation in electron or carbon density.

In the SF-LFS configuration, baffles only slightly reduce Z_{eff} . We expect that while the colder divertor would be more transparent to impurities, the increased divertor closure would simply decrease the probability of impurities entering the core plasma. Comparing with the baffled SN, the baffled SF-LFS configuration exhibits an up to 25% higher Z_{eff} , suggesting stronger core impurity penetration. The SF-LFS case with small $dr_{\text{X}2}$ (not shown here) displays a slightly milder

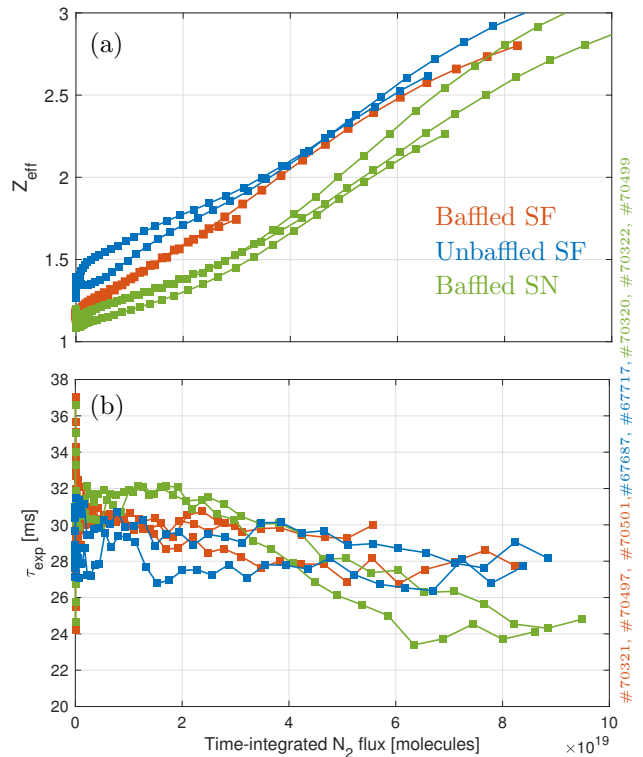


Figure 10: (a) Core effective charge, Z_{eff} , estimated from measurements of V_{loop} and the profile-averaged core temperature from Thomson scattering. (b) Core energy confinement time estimated from Thomson scattering measurements of core plasma density and temperature profiles. Results are shown from repeat discharges in each geometry.

trend, but still with an up to 20% increase in Z_{eff} . In Ne-seeded near-exact SF experiments on TCv, no difference was discerned in the core impurity shielding of the SF and SN [40]. SF- experiments in NSTX observe a reduction in core impurity content during the formation of the SF configuration, but this is attributed to a difference in ELM behaviour rather than the magnetic geometry [41, 42].

The increase in Z_{eff} observed here may signify a SOL in the baffled L-mode SF-LFS that is more transparent to impurities than for the baffled SN. Furthermore, this suggests that a radiation region located further away from the core plasma, figure 8, did not necessarily improve core compatibility. This will need to be explored in future experiments under higher power conditions, where low- Z impurity screening can increase [43].

5.2. Energy confinement time

We now focus on the energy confinement time, τ_{exp} , defined as,

$$\tau_{\text{exp}} = \frac{W_{\text{MHD}}}{P_{\text{in}}}, \quad (4)$$

where W_{MHD} is the plasma stored energy and P_{in} the input heating power, which in this case is only Ohmic. Although diamagnetic loop measurements are often used to measure the stored plasma energy, it is difficult to compensate the flux measurement sensitivity to poloidal magnetic fields [44], which, across the studied configurations, can differ greatly. Here, W_{MHD} is estimated by integrating the core electron temperature and density profiles, from Thomson scattering, over the plasma volume,

$$W_{\text{MHD}} = 2\pi \iint (3n_e T_e) R dR dZ, \quad (5)$$

where R and Z are the poloidal coordinates. We assume $T_i = T_e$ and that impurity densities are in the trace limit. The latter assumption can lead to an overestimation of W_{MHD} by up to 15%. CXRS (Charge eXchange Recombination Spectroscopy) measurements of T_i were only available for a small subset of the data presented, and so are not used, but confirm the trends observed by the assumption $T_i = T_e$.

Figure 10 (b) shows the energy confinement time for the discharges presented in the study. Initially, the baffled SF-LFS shows a slightly lower energy confinement time than the baffled SN (11% at most). As further N_2 is injected, this difference reverses, with the SF-LFS now showing a $\sim 16\%$ increase in τ_{exp} compared to the SN. Snowflake experiments in DIII-D, NSTX and MAST-U find that core confinement is unaffected by the SF geometry in attached conditions [29, 36, 42]. Meanwhile, radiative experiments in DIII-D observe a stronger degradation of stored energy in the SF compared to the SN [35, 45].

The presence of baffles in the SF-LFS does not strongly affect the core confinement (consistent with SN experiments in JT60U [30]). In TCV, we conclude that no strong, systematic difference between the three configurations is discerned in these low density, L-mode experiments. Analysis of SF-LFS discharges at higher plasma density and in H-mode is planned, where the difference in magnetic configuration is expected to have a more significant effect on core confinement.

6. Conclusion

Baffled SF-LFS geometries have been successfully developed on TCV to explore the effect of divertor closure on the power exhaust and divertor-core compatibility of the SF-LFS, compared with standard

baffled SN configurations. In the Ohmic L-mode discharges investigated herein, the SF-LFS shows a peak outer target heat flux reduction of around 20% with baffling, and maintains the inter-null radiation region observed without baffles, with no significant effect on core-divertor compatibility. In these proof-of-principle experiments, the baffled SF-LFS presents promising power exhaust features over the baffled SN in terms of outer target heat flux reductions and balance of strike-point heat flux distribution. However, whilst approaching detachment through injecting N_2 , these differences diminish, with similar target conditions and divertor radiative power losses between the two geometries for the higher N_2 injection rates. Despite a radiation region located further from the confined plasma for the baffled SF-LFS, no meaningful improvement is observed in either core confinement or core effective charge as a function of time-integrated N_2 flux.

The experimental scenarios presented herein form a good reference for detailed model validations and extrapolations, exploring important physics that has not yet been understood from the experimental results alone. Moving forward, ongoing EMC3-EIRENE simulations [46] look to further explore the roles of divertor radiative losses and core impurity shielding in target heat flux mitigation, whilst studying the dependence of divertor cross-field transport on magnetic geometry. In parallel, further experiments will explore the effect of increasing SOL opacity to neutrals, by increasing the separatrix density and input power, to investigate whether the SF-LFS benefits can be maintained while seeding impurities.

Acknowledgments

This work was supported in part by the Swiss National Science Foundation. This work has been carried out within the framework of the EUROfusion Consortium, funded by the European Union via the Euratom Research and Training Programme (Grant Agreement No 101052200 — EUROfusion). Views and opinions expressed are however those of the author(s) only and do not necessarily reflect those of the European Union or the European Commission. Neither the European Union nor the European Commission can be held responsible for them.

Data availability statement

The data used to produce the figures in this article are available at <https://doi.org/10.5281/zenodo.6957736>.

References

- [1] Pitts R A, Bonnin X, Escourbiac F, Frerichs H, Gunn J P, Hirai T, Kukushkin A S, Kaveeva E, Miller M A, Moulton D, Rozhansky V, Senichenkov I, Sytova E, Schmitz O, Stangeby P C, De Temmerman G, Veselova I and Wiesen S 2019 *Nuclear Materials and Energy* **20** 100696 ISSN 23521791 URL <https://doi.org/10.1016/j.nme.2019.100696>
- [2] Leonard A W 2018 *Plasma Physics and Controlled Fusion* **60** ISSN 13616587
- [3] Février O, Reimerdes H, Theiler C, Brida D, Colandrea C, De Oliveira H, Duval B P, Galassi D, Gorno S, Henderson S, Komm M, Labit B, Linehan B, Martinelli L, Perek A, Raj H, Sheikh U, Tsui C K and Wensing M 2021 *Nuclear Materials and Energy* **27** ISSN 23521791
- [4] Reimerdes H, Duval B P, Elaian H, Fasoli A, Février O, Theiler C, Bagnato F, Baquero-Ruiz M, Blanchard P, Brida D, Colandrea C, de Oliveira H, Galassi D, Gorno S, Henderson S, Komm M, Linehan B, Martinelli L, Maurizio R, Moret J M, Perek A, Raj H, Sheikh U, Testa D, Toussaint M, Tsui C K and Wensing M 2021 *Nuclear Fusion* **61** ISSN 17414326
- [5] Reimerdes H, Ambrosino R, Innocente P, Castaldo A, Chmielewski P, Di Gironimo G, Merriman S, Pericoli-Ridolfini V, Aho-Mantilla L, Albanese R, Bufferand H, Calabro G, Ciraolo G, Coster D, Fedorczak N, Ha S, Kembleton R, Lackner K, Loschiavo V P, Lunt T, Marzullo D, Maurizio R, Militello F, Ramogida G, Subba F, Varoutis S, Zagórski R and Zohm H 2020 *Nuclear Fusion* **60** ISSN 17414326
- [6] Soukhanovskii V A 2017 *Plasma Physics and Controlled Fusion* **59** ISSN 13616587
- [7] Theiler C, Lipschultz B, Harrison J, Labit B, Reimerdes H, Tsui C, Vijvers W A, Boedo J A, Duval B P, Elmore S, Innocente P, Kruezi U, Lunt T, Maurizio R, Nespoli F, Sheikh U, Thornton A J, Van Limpt S H, Verhaegh K and Vianello N 2017 *Nuclear Fusion* **57** aa5fb7 ISSN 17414326 URL <https://doi.org/10.1088/1741-4326/aa5fb7>
- [8] Fasoli A, Reimerdes H, Alberti S, Baquero-Ruiz M, Duval B P, Havlikova E, Karpushov A, Moret J M, Toussaint M, Elaian H, Silva M, Theiler C, Vaccaro D and team T 2020 TCV heating and divertor upgrades
- [9] Ryutov D D and Soukhanovskii V A 2015 *Physics of Plasmas* **22** ISSN 10897674 URL <http://dx.doi.org/10.1063/1.4935115>
- [10] Ryutov D D 2007 *Physics of Plasmas* **14** ISSN 1070664X
- [11] Reimerdes H, Canal G P, Duval B P, Labit B, Lunt T, Vijvers W A, Coda S, De Temmerman G, Morgan T W, Nespoli F and Tal B 2013 *Plasma Physics and Controlled Fusion* **55** ISSN 07413335
- [12] Pan O, Lunt T, Wischmeier M, Coster D and Asdex Upgrade Team T 2018 *Plasma Physics and Controlled Fusion* **60** ISSN 13616587
- [13] Giacomini M, Stenger L N and Ricci P 2020 *Nuclear Fusion* **60** ab6435 ISSN 17414326 URL <https://doi.org/10.1088/1741-4326/ab6435>
- [14] Zhang Y, Sang C, Li J, Zheng G, Zhang C, Liu D and Wang D 2020 *Nuclear Materials and Energy* **25** 100803 ISSN 23521791 URL <https://doi.org/10.1016/j.nme.2020.100803>
- [15] Maurizio R, Tsui C K, Duval B P, Reimerdes H, Theiler C, Boedo J, Labit B, Sheikh U and Spolaore M 2019 *Nuclear Fusion* **59** aae1b ISSN 17414326 URL <https://doi.org/10.1088/1741-4326/aae1b>
- [16] Labit B, Canal G P, Christen N, Duval B P, Lipschultz B, Lunt T, Nespoli F, Reimerdes H, Sheikh U, Theiler C, Tsui C K, Verhaegh K and Vijvers W A 2017 *Nuclear Materials and Energy* **12** 1015–1019 ISSN 23521791 URL <https://doi.org/10.1016/j.nme.2017.03.013>
- [17] Bernert M, Wischmeier M, Huber A, Reimold F, Lipschultz B, Lowry C, Brezinsek S, Dux R, Eich T, Kallenbach A, Lebschy A, Maggi C, McDermott R, Pütterich T and Wiesen S 2017 *Nuclear Materials and Energy* **12** 111–118 ISSN 23521791 URL <https://doi.org/10.1016/j.nme.2016.12.029>
- [18] Bernert M, Janky F, Sieglin B, Kallenbach A, Lipschultz B, Reimold F, Wischmeier M, Cavedon M, David P, Dunne M G, Griener M, Kudlacek O, McDermott R M, Treutterer W, Wolfrum E, Brida D, Février O, Henderson S and Komm M 2021 *Nuclear Fusion* **61** ISSN 17414326
- [19] Février O, Theiler C, Harrison J R, Tsui C K, Verhaegh K, Wüthrich C, Boedo J A, De Oliveira H, Duval B P, Labit B, Lipschultz B, Maurizio R and Reimerdes H 2020 *Plasma Physics and Controlled Fusion* **62** 35017 ISSN 13616587 URL <http://dx.doi.org/10.1088/1361-6587/ab6b00>
- [20] Reimerdes H, Duval B P, Harrison J R, Labit B, Lipschultz B, Lunt T, Theiler C, Tsui C K, Verhaegh K, Vijvers W A, Boedo J A, Calabro G, Crisanti F, Innocente P, Maurizio R, Pericoli V, Sheikh U, Spolare M and Vianello N 2017 *Nuclear Fusion* **57** aa82c2 ISSN 17414326 URL <https://doi.org/10.1088/1741-4326/aa82c2>
- [21] Siccini M, Federici G, Kembleton R, Lux H, Maviglia F and Morris J 2019 *Nuclear Fusion* **59** ISSN 17414326
- [22] Raj H, Theiler C, Thornton A, Février O, Gorno S, Bagnato F, Blanchard P, Colandrea C, de Oliveira H, Duval B, Labit B, Perek A, Reimerdes H, Sheikh U, Vallar M, Vincent B, Team T T and Team T E M 2022 *Submitted to Nuclear Fusion*
- [23] Maurizio R, Elmore S, Fedorczak N, Gallo A, Reimerdes H, Labit B, Theiler C, Tsui C K and Vijvers W A 2018 *Nuclear Fusion* **58** aa986b ISSN 17414326 URL <https://doi.org/10.1088/1741-4326/aa986b>
- [24] Février O, Theiler C, De Oliveira H, Labit B, Fedorczak N and Baillod A 2018 *Review of Scientific Instruments* **89** ISSN 10897623 URL <http://dx.doi.org/10.1063/1.5022459>
- [25] De Oliveira H, Marmillod P, Theiler C, Chavan R, Février O, Labit B, Lavanchy P, Marlétaz B and Pitts R A 2019 *Review of Scientific Instruments* **90** ISSN 10897623 URL <https://doi.org/10.1063/1.5108876>
- [26] Brida D, Silvagni D, Eich T, Faitsch M and McCarthy P 2020 *Plasma Physics and Controlled Fusion* **62** ISSN 13616587
- [27] Sheikh U A, Simons L, Duval B, Février O, Moret D, Allegrucci A, Bernert M, Crisinel F, Tertszyanszky T and Villinger O 2022 *Submitted to Review of Scientific Instruments*
- [28] Galassi D, Reimerdes H, Theiler C, Wensing M, Bufferand H, Ciraolo G, Innocente P, Marandet Y and Tamain P 2020 *Plasma Physics and Controlled Fusion* **62** ISSN 13616587
- [29] Soukhanovskii V A, Bell R E, Diallo A, Gerhardt S, Kaye S, Kolenen E, Leblanc B P, McLean A G, Menard J E, Paul S F, Podesta M, Raman R, Roglien T D, Roquemore A L, Ryutov D D, Scotti F, Umansky M V, Battaglia D, Bell M G, Gates D A, Kaita R, Maingi R, Mueller D and Sabbagh S A 2012 *Physics of Plasmas* **19** ISSN 1070664X
- [30] Asakura N, Hosogane N, Itami K, Sakasai A, Sakurai S, Shimizu K, Shimada M, Kubo H, Higashijima S, Takenaga H, Tamai H, Konoshima S, Sugie T, Masaki K, Koide Y, Naito O, Shirai H, Takizuka T, Ishijima T, Suzuki S and Kumagai A 1999 *Journal of Nuclear Materials* **266** 182–188 ISSN 00223115
- [31] Lipschultz B, LaBombard B, Terry J L, Boswell C and Hutchinson I H 2007 *Fusion Science and Technology* **51**

- 369–389 ISSN 15361055
- [32] Kallenbach A, Bernert M, Beurskens M, Casali L, Dunne M, Eich T, Giannone L, Herrmann A, Maraschek M, Potzel S, Reimold F, Rohde V, Schweinzer J, Viezzer E and Wischmeier M 2015 *Nuclear Fusion* **55** 53026 ISSN 17414326 URL <http://dx.doi.org/10.1088/0029-5515/55/5/053026>
- [33] Ohno N, Tanaka N, Ezumi N, Nishijima D and Takamura S 2001 *Contributions to Plasma Physics* **41** 473–480 ISSN 08631042
- [34] Kamleitner J 2015 *Suprathermal electron studies in Tokamak plasmas by means of diagnostic measurements and modeling* Ph.D. thesis EPFL
- [35] Soukhanovskii V A, Allen S L, Fenstermacher M E, Lasnier C J, Makowski M A, McLean A G, Meyer W H, Ryutov D D, Kolemen E, Groebner R J, Hyatt A W, Leonard A W, Osborne T H, Petrie T W and Watkins J 2018 *Nuclear Fusion* **58** aaa6de ISSN 17414326 URL <https://doi.org/10.1088/1741-4326/aaa6de>
- [36] Soukhanovskii V A, Cunningham G, Harrison J R, Federici F and Ryan P 2022 *Nuclear Materials and Energy* **33** ISSN 23521791
- [37] Soukhanovskii V A, Allen S L, Fenstermacher M E, Hill D N, Lasnier C J, Makowski M A, Mclean A G, Meyer W H, Kolemen E, Groebner R J, Hyatt A W, Leonard A W, Osborne T H and Petrie T W 2015 *Journal of Nuclear Materials* **463** 1191–1195 ISSN 00223115 URL <http://dx.doi.org/10.1016/j.jnucmat.2014.12.052>
- [38] Sauter O, Angioni C and Lin-Liu Y R 1999 *Physics of Plasmas* **6** 2834 ISSN 1070664X
- [39] Sauter O, Angioni C, Coda S, Gomez P, Goodman T P, Henderson M A, Hofmann F, Hogge J P, Moret J M, Nikkola P, Pietrzyk Z A, Weisen H, Alberti S, Appert K, Bakos J, Behn R, Blanchard P, Bosshard P, Chavan R, Condrea I, Degeling A, Duval B P, Fasel D, Favez J Y, Favre A, Furno I, Kayruthdinov R R, Lavanchy P, Lister J B, Llobet X, Lukash V E, Gorgerat P, Isoz P F, Joye B, Magnin J C, Manini A, Marlétaz B, Marmillod P, Martin Y R, Martynov A, Mayor J M, Minardi E, Mlynar J, Paris P J, Perez A, Peysson Y, Piffi V, Pitts R A, Pochelon A, Reimerdes H, Rommers J H, Scavino E, Sushkov A, Tonetti G, Tran M Q and Zabolotsky A 2001 *Physics of Plasmas* **8** 2199–2207 ISSN 1070664X
- [40] Reimerdes H, Canal G P, Duval B P, Labit B, Lunt T, Nespoli F, Vijvers W A, De Temmerman G, Lowry C, Morgan T W, Tal B and Wischmeier M 2015 *Journal of Nuclear Materials* **463** 1196–1199 ISSN 00223115
- [41] Soukhanovskii V A, Ahn J W, Bell R E, Gates D A, Gerhardt S, Kaita R, Kolemen E, LeBlanc B P, Maingi R, Makowski M, Maqueda R, McLean A G, Menard J E, Mueller D, Paul S F, Raman R, Roquemore A L, Ryutov D D, Sabbagh S A and Scott H A 2011 *Nuclear Fusion* **51** ISSN 00295515
- [42] Soukhanovskii V A, Allen S L, Fenstermacher M E, Lasnier C J, Makowski M A, McLean A G, Meier E T, Meyer W H, Roglien T D, Ryutov D D, Scotti F, Kolemen E, Bell R E, Diallo A, Gerhardt S, Kaita R, Kaye S, LeBlanc B P, Maingi R, Menard J E, Podesta M, Roquemore A L, Groebner R J, Hyatt A W, Leonard A W, Osborne T H, Petrie T W, Ahn J W, Raman R and Watkins J G 2016 *IEEE Transactions on Plasma Science* **44** 3445–3455 ISSN 00933813
- [43] Mccracken G M, Lipschultz B, Labombard B, Goetz J A, Granetz R S, Jablonski D, Lisgo S, Ohkawa H, Stangeby P C and Terry J L 1997 *Physics of Plasmas* **4** 1681–1689 ISSN 10897674
- [44] Manini A, Moret J M, Alberti S, Goodman T P and Henderson M A 2002 *Plasma Physics and Controlled Fusion* **44** 139–157 ISSN 07413335
- [45] Hill D N 2013 *Nuclear Fusion* **53** ISSN 00295515
- [46] Lunt T, Canal G P, Duval B P, Feng Y, Labit B, McCarthy P, Reimerdes H, Vijvers W A and Wischmeier M 2016 *Plasma Physics and Controlled Fusion* **58** ISSN 13616587